J. Fluid Mech. (1995), *vol.* 299, *pp.* 267–288

A numerical study of the wave-induced solute transport above a rippled bed

By K. T. SHUM †

Maurice Lamontagne Institute, Department of Fisheries & Oceans, Mont-Joli, Québec, Canada G5H 3Z4

(Received 25 January 1994 and in revised form 4 April 1995)

The role of wave-induced separated flow in solute transport above a rippled bed is studied from numerical solutions to the two-dimensional Navier–Stokes equations and the advection–diffusion equation. A horizontal ambient flow that varies sinusoidally in time is imposed far above the bed, and a constant concentration difference between the upper and lower boundaries of computation is assumed. The computed flow field is the sum of an oscillatory rectilinear flow and a vortical flow which is periodic both in time and in the horizontal. Poincaré sections of this flow suggest chaotic mixing. Vertical lines of fluid particles above the crest and above the trough deform into whorls and tendrils, respectively, in just one wave period. Horizontal lines near the bottom deform into Smale horseshoe patterns. The combination of high shear and vortex-induced normal velocity close to the sediment surface results in large net displacements of fluid particles in a period. The resulting advective transport normal to the bed can be higher than molecular diffusion from well within the viscous boundary layer up to a few ripple heights above the bed. When this flow field is applied to the transport equation of a passive scalar, two distinct features – regular temporal oscillations in concentration and a linear time-averaged vertical concentration profile – are found immediately above the bed. These features have also been observed previously in field measurements on oxygen concentration. Advective transport is shown to be dominant even in the region where the time-averaged concentration profile is linear, a region where vertical solute transport has often been estimated using diffusion-type models in many field studies.

1. Introduction

The remineralization of detrital organic matter by bacteria in marine sediments is an important link in the global carbon cycle. Many remineralization processes can progress only in the presence of oxygen, and are therefore dependent on the oxygen flux from the oxygen-rich water into the oxygen-poor pore water in the sediments.

Coastal sediments are often sandy with uneven surfaces such that the flows above are usually separated. Such vortical flows, generated for example when the ambient water is induced into oscillatory motion under surface gravity waves, provide an efficient mixing mechanism immediately above the sediment bed and enhance the vertical transport of dissolved substances from the water column into interstitial pore water.

† Present address: Contra Costa Water District, 1331 Concord Avenue, PO Box H20, Concord, CA 94524, USA.

Gundersen & Jørgensen (1990) measured the vertical distribution of oxygen at the sediment–water interface in water 15 m deep. They found that the time-averaged concentration was indeed nearly constant except in a thin layer immediately above the sediment surface, where the mean concentration decreased linearly with decreasing elevation. Within this layer, which was about 0.6 mm thick, molecular diffusion was believed to be the dominant transport mechanism and a diffusion-type transport model was used to estimate the vertical flux of solutes. However, comparisons with actual flux measurements suggested that such an 'empirical diffusion coefficient' would have to be a few times higher than that of molecular diffusivity.

Interestingly, the oxygen concentration in the middle of this 'diffusive boundary layer' (DBL) oscillated in time with a magnitude of more than 10% of its mean value and at the frequency of the prevalent surface gravity wave. As the length scale of molecular diffusion of oxygen (with a diffusivity typically of 10^{-9} m^2s^{-1}) over a wave period was considerably smaller than the thickness of the DBL, diffusive transport alone could not explain such temporal variations. Another plausible explanation, that due to percolation, could only account for oscillations at a much smaller magnitude due to the small wave-induced pore water flow. Gundersen & Jørgensen (1990) attributed the oscillations to 'numerous eddies which approach the sediment surface from the bulk of the flowing sea water and hit the viscous and diffusive sublayers', but details of the physical mechanism involved had not been explored. More importantly, if the effects of ambient vortices were prominent in the DBL, would a diffusive-type transport model be adequate to describe the vertical flux of solutes?

Aside from ambient turbulence, vortical motions close to the sediment bed may also be due to flow separations at the lower boundary caused by small-scale surface topography under the actions of gravity waves and currents. Among the different forms of surface roughness, sand ripples are probably the most common in coastal sediments, and their often periodic and two-dimensional profiles under a wide range of flow regimes are particularly conducive to analytical treatment. To investigate the effects of vortical motions on vertical solute transport immediately above a sediment bed, a periodic ripple profile will therefore be assumed in this study as an illustrative example of the effects of bottom roughness.

Even though the flow over sand ripples induced by the passage of gravity waves has received much attention (see for example the review of Mei & Liu 1993), analytical studies on the transport immediately above a rippled surface are few and have been limited to two-dimensional unidirectional flows. These include the empirical turbulence transport model of Thorsness & Hanratty (1979) and the numerical solutions of Vittori & Tanda (1991), with the latter on the slightly different case of a channel with horizontal wavy walls at the bottom. For oscillatory flows but under slightly different physical setups, Sobey (1985) simulated the dispersion of fluid particles in a furrowed channel and Ghaddar *et al.* (1986) analysed the enhanced heat transfer in a rectangular grooved channel. Both studies solved the flow and transport equations numerically. Owing to the differences in the physical systems, these results cannot be applied directly to the wave-induced vertical transport in the benthic boundary.

The flow field above a sediment bed is always turbulent. However, flow separations and persistent vortical motions, the dominant features in wave-induced oscillatory flows over sand ripples, have been found to be prominent even when the ambient flow is much weaker such that the flow field is amenable to numerical simulations (Blondeaux & Vittori 1991*a*). Such deterministic flow fields, despite their relatively simple features, can lead to chaotic mixing (Ottino 1989). In a physical setup that shares many of the same characteristics, Sobey (1985) has shown numerically that

an initial blob of particles would indeed disperse in a complicated pattern when the oscillatory flow in a furrowed channel is separated.

To gain a better understanding on the solute transport in a wave-induced separated boundary flow, numerical solutions to the Navier–Stokes equations and the transport equation will be analysed in the following. A two-dimensional flow field bounded below by rigid and spatially periodic ripples is driven by an imposed oscillatory ambient flow. Ambient turbulence is not modelled and the only vortical flows originate from separations at the bottom boundary. This assumption is consistent with the observations of Gundersen & Jørgensen (1990) since oscillations in concentration at the wave frequency suggest that boundary-generated vortical flow, rather than random ambient turbulence, is at work. As truncation errors of the advective terms exceed molecular diffusion at low diffusivity and therefore limit the range of validity of the numerical solution to the transport equation, the kinematics of the computed flow field is analysed to infer the nature of solute transport at low diffusivities (the molecular diffusivity of oxygen, and those of many other solutes of practical interest, are typically 10^{-3} that of kinematic viscosity). I aim to explain the mechanisms leading to the temporal fluctuations in solute concentration and quantify the magnitude of vertical transport of dissolved substances close to the sediment surface.

The formulation and numerical procedures are outlined only briefly in §§2 and 3 as they have been reported elsewhere. In §§4 and 5 the flow field of interest and the corresponding concentration field for a case of high molecular diffusivity are presented. Extension to low molecular diffusivity is inferred from the kinematics of the flow field in §6. The relevance of these results to benthic transport processes is discussed in §7.

2. Formulation

A semi-infinite Newtonian fluid of constant density is driven by an imposed oscillatory pressure gradient above a rippled bed with a periodic profile. Navier–Stokes equations in two dimensions are solved numerically in terms of streamfunction ψ and vorticity ω in the vertical strip between two adjacent ripple crests and truncated sufficiently high above the bed. The computational domain (x, y) is a rectangle mapped conformally onto the physical plane $(\tilde{x}, \tilde{y})$ in nondimensionalized coordinates. This flow model is identical to that in Shum (1988) and Blondeaux & Vittori (1991*a*,*b*).

All physical variables are nondimensionalized with the ripple length L, period and amplitude of the ambient oscillatory velocity T and U, and concentration at the upper boundary c_0. The streamfunction is scaled with UL and vorticity with U/L. The governing equations in the transformed plane take the form

$$J\frac{\partial\omega}{\partial t}+\frac{\pi}{S}\left(\frac{\partial\psi}{\partial y}\frac{\partial\omega}{\partial x}-\frac{\partial\psi}{\partial x}\frac{\partial\omega}{\partial y}\right)=\frac{\pi}{RS}\left(\frac{\partial^2\omega}{\partial x^2}+\frac{\partial^2\omega}{\partial y^2}\right), \tag{2.1}$$

$$\frac{\partial^2\psi}{\partial x^2}+\frac{\partial^2\psi}{\partial y^2}=-J\omega, \tag{2.2}$$

and

$$J\frac{\partial c}{\partial t}+\frac{\pi}{S}\left(\frac{\partial\psi}{\partial y}\frac{\partial c}{\partial x}-\frac{\partial\psi}{\partial x}\frac{\partial c}{\partial y}\right)=\frac{\pi}{PRS}\left(\frac{\partial^2 c}{\partial x^2}+\frac{\partial^2 c}{\partial y^2}\right), \tag{2.3}$$

where

$$J(x,y) = \begin{vmatrix} \dfrac{\partial \tilde{x}}{\partial x} & \dfrac{\partial \tilde{x}}{\partial y} \\ \dfrac{\partial \tilde{y}}{\partial x} & \dfrac{\partial \tilde{y}}{\partial y} \end{vmatrix} \tag{2.4}$$

is the Jacobian of transformation and variables t and c are respectively time and concentration. The dimensionless parameters

$$S = \pi L/UT = L/A, \quad R = UL/\nu, \quad P = \nu/\kappa \tag{2.5a–c}$$

are respectively the Strouhal number, Reynolds number, and Prandtl number. The variables ν and κ are the laminar viscosity and molecular diffusivity, respectively. For a simple harmonic ambient flow, $A = UT/\pi$ where A is the magnitude of displacement of a fluid particle in the far field. Note that, by assuming the effects of solute concentration on fluid density to be negligible, the solution to the flow equations (2.1) and (2.2) is not dependent on the solution to the transport equation (2.3).

The bottom boundary is spatially periodic and defined by

$$\{\tilde{x}_r(x),\ \tilde{y}_r[\tilde{x}_r(x)]\} = \left(x - \frac{1}{2}s\sin 2\pi x,\ \frac{1}{2}s\cos 2\pi x\right) \tag{2.6}$$

where $s = 2a/L$ is the mean ripple steepness (πs is the maximum slope in the profile) and a is half the ripple height. This profile closely resembles sand ripples generated in the laboratory (Du Toi & Sleath 1981). The corresponding conformal mapping is (Benjamin 1959)

$$\begin{Bmatrix} \tilde{x} \\ \tilde{y} \end{Bmatrix} = \begin{Bmatrix} x - \frac{1}{2}s\exp(-2\pi y)\sin 2\pi x \\ y + \frac{1}{2}s\exp(-2\pi y)\cos 2\pi x \end{Bmatrix} \tag{2.7}$$

and the Jacobian is

$$J = 1 + \pi^2 s^2 \exp(-4\pi y) - 2\pi s \exp(-2\pi y)\cos 2\pi x. \tag{2.8}$$

The bottom boundary conditions on the ripple surface $y = 0$ are

$$\psi = \frac{\partial \psi}{\partial y} = 0 \quad \text{and} \quad c = 0. \tag{2.9a,b}$$

The flow field is forced by small-amplitude gravity waves with a wavelength and a water depth assumed to be much greater than the ripple length. The wave-induced velocity and horizontal pressure gradient near bottom can then be approximated as sinusoidal in time and independent of x. The concentration is assumed constant high above the bottom boundary. The conditions at the upper boundary $y = y_{max}$ of the truncated computational domain are therefore

$$\frac{\partial \psi}{\partial x} = 0, \quad \frac{\partial \psi}{\partial y} = U_\infty(t) = \sin 2\pi t, \quad \text{and} \quad c = 1. \tag{2.10a–c}$$

Note that (2.10) implicitly imposes an oscillatory pressure gradient in the horizontal that would drive the ambient fluid with velocity $U_\infty(t)$ high above the bed.† This pressure gradient provides the forcing mechanism and leads to a viscid layer only at the bottom boundary.

† A derivation of this equivalence is given in the Appendix.

The boundary conditions (2.10) are imposed at the top of the computational domain instead of at $y \to \infty$, even though the latter would correspond directly to the physical problem. To define boundary concentration at $y \to \infty$ would require, in order to maintain a downward flux of solute, that $c \to \alpha y$ or the transport equation (2.3) be modified to allow for some kind of 'turbulent transport'. To avoid these options, the boundary conditions (2.10) are defined at $y = y_{max}$ instead for expediency.

The flow field and concentration field are assumed to be periodic in x such that

$$\psi(x = 0, y, t) = \psi(x = 1, y, t) \tag{2.11a}$$

and

$$c(x = 0, y, t) = c(x = 1, y, t). \tag{2.11b}$$

3. Numerical algorithm

The numerical scheme for (2.1) and (2.2) has been discussed in detail in Shum (1988). A pseudo-spectral (collocation) method is used in which derivatives in x are computed in the Fourier space while the nonlinear terms are evaluated in the physical space. Derivatives in y are computed by second-order centred-differencing. Time stepping is through a split-step-type scheme with the convective terms in the vorticity equation simulated by a third-order Adams–Bashforth scheme and the viscous terms by an Euler forward scheme. The Poisson equation (2.2) is solved in the Fourier space by compact differencing.

Even though this scheme shares many of the features in the simulations of Blondeaux & Vittori (1991*a*,*b*), there are a few differences. In their papers, Euler forward was used for the advective terms, the y-derivatives in the Poisson equation were simulated with second-order centred-differencing, and a dealiasing scheme was used for the spectral derivatives.

To verify the accuracy of the numerical scheme, solutions of (2.1) and (2.2) for closely related flows have been compared quantitatively with solutions obtained analytically or numerically. This includes the exact solution for the impulsively started oscillatory flow over a plane bed (Carslaw & Jaeger 1963, §47, p.110), the numerical solution for the flow around an impulsively started circular cylinder based on a finite-differencing scheme (Ta Phuoc Loc 1980), and the asymptotic solution to the oscillatory flow above a rippled bed for $R = 630, S = \pi/4$, and $s = 0.1$ (Hara & Mei 1992). Good agreements were found in all these comparisons. Details can be found in Shum (1988).

Lagrangian particle tracking in the flow field with velocity components $(\psi_y, -\psi_x)$ is performed using Euler forward with linear interpolation in space. Time-steps of $\approx O(10^3)$ to $O(10^4)$ per wave period are used, and the convergence of these solutions is confirmed from computations using different time steps.

The numerical scheme for the transport equation (2.3) is the same as that in (2.1). The numerical solutions have also been compared with the solutions to the conservative form (Anderson, Tannehill & Pletcher 1984)

$$J\frac{\partial c}{\partial t} + \frac{\pi}{S}\left[\frac{\partial}{\partial x}\left(c\frac{\partial \psi}{\partial y}\right) - \frac{\partial}{\partial y}\left(c\frac{\partial \psi}{\partial x}\right)\right] = \frac{\pi}{PRS}\left(\frac{\partial^2 c}{\partial x^2} + \frac{\partial^2 c}{\partial y^2}\right). \tag{3.1}$$

The discrepancies between the two solutions are small (under 3%).

The flow at the start of computation is that of an oscillatory flow in the mapped plane (Stokes second problem, Schlichting 1968, §V.7, p.93). The solution to (2.1) and

(2.2) with $J \equiv 1$ is assumed, that is,

$$\psi_s(x, y, t) = y \sin 2\pi t - \frac{1}{\beta\sqrt{2}}\left[\exp(-\beta y)\cos\left(2\pi t - \beta y + \frac{\pi}{4}\right) - \cos\left(2\pi t + \frac{\pi}{4}\right)\right] \tag{3.2}$$

evaluated at $t = 0$, where $\beta = (RS)^{1/2}$. Note the phase lead of ψ_s at small y. An initial linear concentration profile

$$c_s\,(x, y, t = 0) = y/y_{max} \tag{3.3}$$

is also assumed.

A non-uniform grid is used in the vertical and the grid size increases exponentially with y. Grid spacings at the bottom boundary are set to be a fraction of the diffusive boundary layer thickness over a flat bed, which is of the order of $(\kappa T)^{1/2}/L = (\pi/PRS)^{1/2}$. The same 32×109 grid with $y_{max} = 3$ is used in the computations of (2.1), (2.2) and (2.3). The upper boundary is confirmed *a posteriori* to be well above the vertical extent of the vortical flow. Computations are performed in 64-bit real numbers.

In the solutions reported below, the Fourier spectra of the vorticity have been examined to ensure that aliasing effects are small in the computations of nonlinear terms in (2.1) and (2.3), and that all Fourier components with nonzero wavenumbers vanish close to the upper boundary. In addition, momentum balance and mass balance of solutes over the computational domain are used as global checks of numerical accuracy as follows. The discrepancies in the conservation equations for momentum and mass of solutes are computed from the numerical solutions. These discrepancies, which give estimates of the numerical errors, are compared with the magnitudes of individual terms in the momentum and mass balance equations. These magnitudes are computed with $\psi - \psi_s$ and $c - c_s$, where ψ_s is the streamfunction for Stokes flow (3.2) and c_s is the linear concentration profile (3.3). In both cases, the discrepancies are always under 1% of the magnitudes. (This percentage error would have been much smaller if the discrepancy is compared with the magnitudes of ψ and c as the vortices-induced flow is much weaker than the ambient oscillatory flow.) Details of the accuracy checks in the computation of the flow field have been discussed in Shum (1988).

4. Flow field

Numerically computed oscillatory flows over spatially periodic ripples have been discussed in Shum (1988) and Blondeaux & Vittori (1991*a*,*b*) over a range of dimensionless parameters R, S and s. The flow field ranges from being periodic in time and symmetric over the two halves of a wave period at low dimensionless numbers, to periodic but asymmetric as these numbers increase, to aperiodic (and asymmetric) at higher dimensionless numbers. Here, symmetry in the flow field is defined as

$$\psi\left(1 - x, y, t + \tfrac{1}{2}\right) = -\psi\,(x, y, t), \tag{4.1}$$

that is, the flow at any time in the second half-period is a mirror image (about a vertical through the ripple crest or through the ripple trough) of the corresponding instant in the first half-period. Recall that the numerical algorithm (spectral method in x) imposes a spatial periodicity of one ripple length in the horizontal.

When the Strouhal number is not much smaller than unity and the values of s and R are moderate (≈ 0.1 and $\approx 10^3$, respectively), one vortex is generated in each half

of a wave period and two counter-rotating vortices are found close to the rippled bed at all times. These vortices drift horizontally with the ambient flow, with one of the pair merging with the newly generated vortex in each half-period. As R increases, vortices generated previously are not dissipated immediately, nor do they always merge with existing vortices. This leads to a fairly complicated flow pattern with multiple vortices found further above the bed. These vortices can have significant influence on the dynamics of each other, and they also modify the conditions under which new vortices are generated. Consequently, the flow field differs from one wave period to the next, and aperiodic solutions are found at high R even after many periods of computations.

A relatively simple flow field with moderate dimensionless numbers is used in this study to explore the transport properties of a separated flow. The Strouhal number is unity such that the magnitude of displacement of a fluid particle far above the bed is one ripple length. Note, however, that the movements of the vortices near the bed are quite different from the water motion in the far field. Simulations with nonintegral multiples of S have resulted in flow fields which are qualitatively similar, and have been discussed in Blondeaux & Vittori (1991*a*) and Shum (1988). The Reynolds number $R = 1250$ is chosen such that the solution is time-periodic but slightly asymmetric, where symmetry is as defined in (4.1). The mean ripple steepness s is 0.1. Time periodicity allows analysis using Poincaré sections. The thickness of the 'Stokes boundary layer' in this case is

$$O\left(\frac{\delta_s}{L}\right) \approx \frac{(\nu T)^{1/2}}{L} = \left(\frac{\pi}{RS}\right)^{1/2} = 0.05. \tag{4.2}$$

Computations for $P = 10^3$ were initially planned and the vertical grid is chosen accordingly to resolve the diffusive boundary layer. The vertical grid spacing at the ripple surface is therefore scaled with $O(\delta_c/L)$ where

$$O\left(\frac{\delta_c}{L}\right) \approx \frac{(\kappa T)^{1/2}}{L} = O\left(\frac{\delta_s}{LP^{1/2}}\right) = \left(\frac{\pi}{PRS}\right)^{1/2}, \tag{4.3}$$

which is around 1.6×10^{-3} for $P = 10^3$, and increases exponentially from 3.3×10^{-4} to 9.9×10^{-2} at the upper boundary.† The time step is determined from the von Neumann criteria and is around 6×10^{-6}.

In the following, the velocity field in the twenty-seventh period of computation is used. At this time, the maximum variation in streamfunction value at any grid point from that at the same phase in the twenty-sixth period is less than 2×10^{-5}.

Figure 1 shows the periodic flow field in the first half of the wave period when the ambient flow is from right to left. The streamfunction shown is $\psi - \psi_s$, the difference between the computed flow and the Stokes flow ψ_s, (3.2). Two distinct vortices with opposite circulations are present above each ripple throughout the half-period, reaching up to close to a ripple length above the rippled bed and advect horizontally with the ambient flow. At the start of the wave period ($U = 0$ at $t = 26$, figure 1*a*), the vortex to the left of the ripple crest (labelled R) is stronger and closer to the bed. It has an anti-clockwise rotation and has just merged with the vortex generated in the preceding half-period. The high velocity gradient between this vortex and the ripple surface adds to the vertical shear of the Stokes flow ψ_s, which is in the same direction at the time.

† Fourier spectra of the computed concentration field for $P \geqslant 10$ showed that 32 grid points in x gave inadequate resolution. These results are therefore not presented.

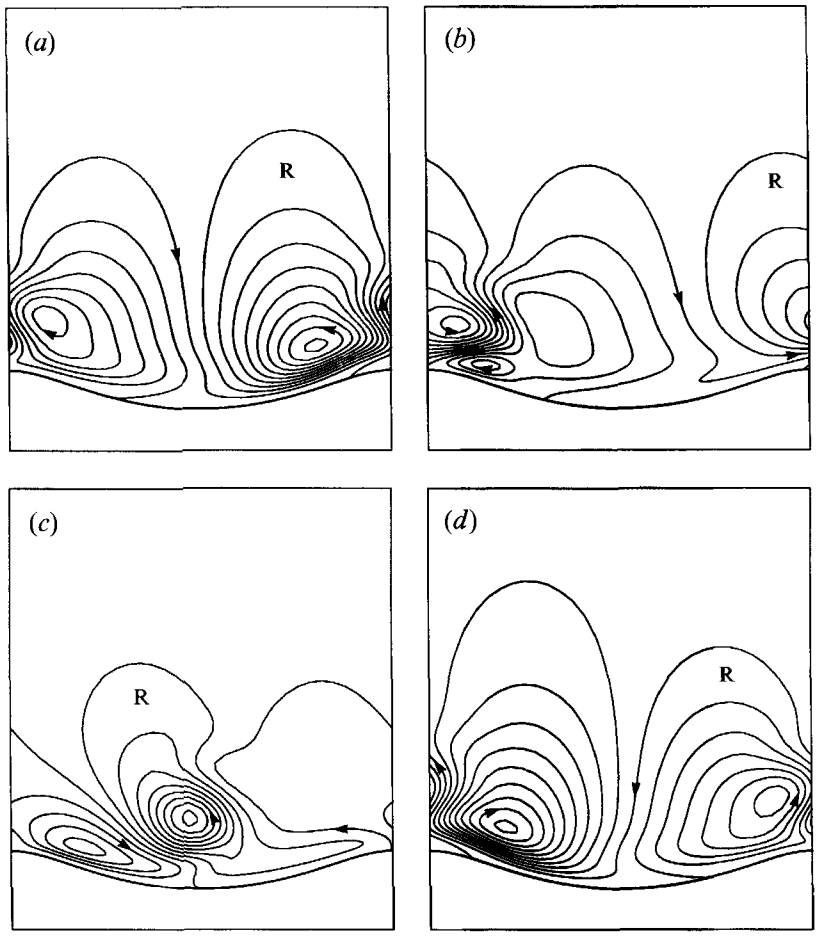

FIGURE 1. Contours of streamfunction $\psi - \psi_s$ over the first half of a wave period for $s = 0.1$, $R = 1250$ and $S = 1$. The results shown are for the twenty-seventh wave period, and the computation starts with the flow field ψ_s. The streamfunction ψ is the computed flow and $\psi_s = \psi_s(y,t)$ is the oscillatory rectilinear flow in the mapped plane (3.2). The flow field is periodic in time at the frequency of ambient oscillations and spatially periodic over one ripple length. The contour interval is $\Delta\psi = 0.015$. The ambient flow $U(t)$ is from left to right and R marks the anti-clockwise vortex initially at the left of a ripple crest at the beginning of the wave period. (*a*) $U = 0$, $t = 0$(modulo 1); (*b*) $U = 1/\sqrt{2}$, $t = 0.125$(modulo 1); (*c*) $U = 1$, $t = 0.25$(modulo 1); (*d*) $U = 0$, $t = 0.5$(modulo 1).

Both vortices advect to the right as the ambient flow increases in that direction, with a new vortex developing at the lee of the ripple crest (figure 1*b*). By the time ambient velocity attains its maximum, the new vortex has merged with the existing one with the same rotation (figure 1*c*) such that at the end of the half-period (figure 1*d*), two vortices are once again found over a ripple length. The vortex to the right of the ripple crest is now the stronger one, and the flow is slightly asymmetric to that at the beginning of the half-period. As the ambient flow reverses in direction, the vortices evolve in a manner similar to that in the previous half-period.

As the two vortices with opposite rotations move back and forth above the ripple surface, they churn up the fluid close to the bottom in a way similar to the two rotating whisks of an electric mixer. The coupling of the high shear between the

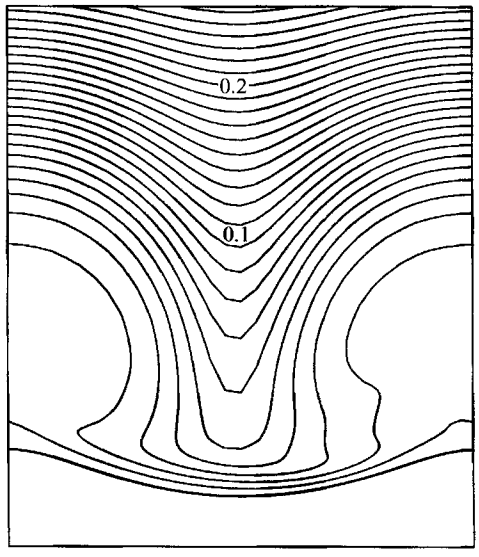

FIGURE 2. Contour plot of the concentration field at the end of 123 periods of computation ($t = 0$, modulo 1) starting with a linear concentration profile in y (3.3) for $s = 0.1$, $R = 1250$, $S = 1$, and $P = 1$. The contour values increase from zero at the ripple surface to 0.26 at the top at regular intervals of 0.01. The concentration field is spatially periodic over one ripple length and time periodic at the wave frequency. The computational domain is approximately three ripple lengths in height but only the bottom third is shown.

vortices and the ripple surface and the normal velocity of fluid particles induced by the vortical flow leads to an efficient mixing mechanism.

5. Concentration field

The concentration field computed from the transport equation (2.3) with $P = 1$ is examined in this section as an illustration of the mixing characteristics of the flow field discussed in the previous section. The flow field is time-periodic and the numerical solution for $26 \leqslant t \leqslant 27$ is used. The time step used in solving the transport equation is $O(10^{-5})$ and the velocity field is linearly interpolated in time from data at some 2200 instants over the wave period. The concentration field discussed below is that after 122 wave periods of computation starting from the linear concentration profile (3.3). At this time the concentration field is nearly time-periodic, and the maximum difference in concentration at any grid point from that at the same phase in the previous wave period is less than 10^{-4}.

The effects of vortical motions on solute distribution are evident in the contour plot of the concentration field (figure 2, $t = 123$). The vortices with opposite rotations induce downward fluid motion in the region above the ripple trough (compare with figure 1*a*). This brings fluid at high solute concentration towards the ripple surface, and at the same time fluid at low solute concentration close to the crest is transported upwards, resulting in the concentration pattern shown. As the vortices move back and forth above the rippled bed, the concentration contours are displaced accordingly. This temporal variation of the solute distribution is straightforward and therefore concentration contours at other times will not be shown. Further above the bed, the concentration is close to the initial distribution (3.3) as the vortical motion there is weak and the concentration contours remain horizontal.

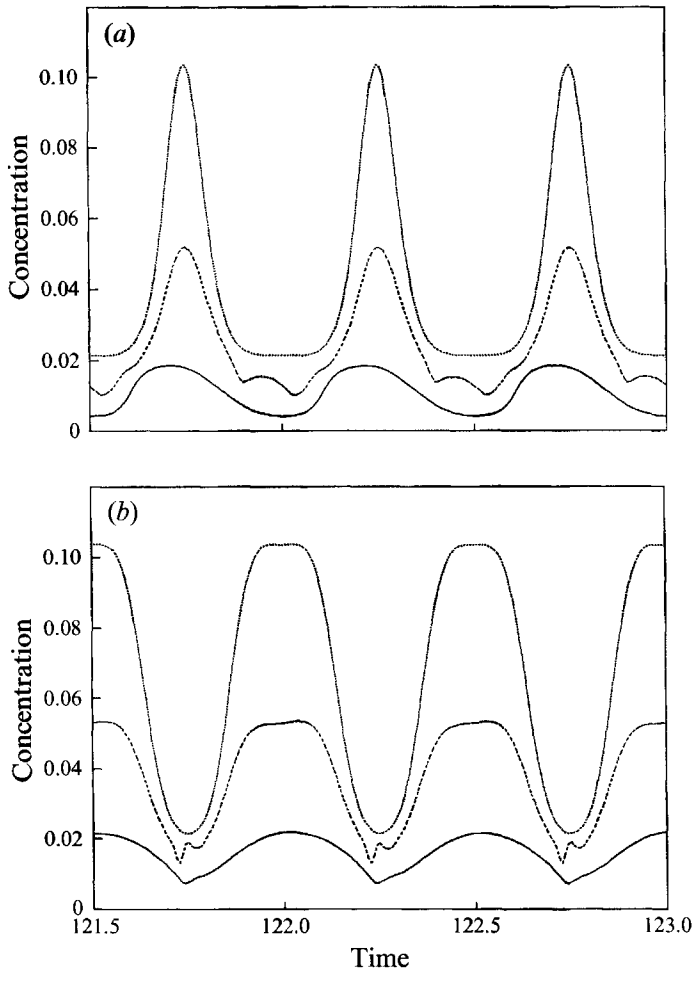

FIGURE 3. Variations of local concentration values with time at $y = 0.025$, 0.1 and 0.5 for $s = 0.1$, $R = 1250$, $S = 1$, and $P = 1$. The concentrations are, for the curves from top to bottom (*a*) at 0.457, 0.076, and 0.018 ripple lengths above the ripple crest; and (*b*) at 0.552, 0.123, and 0.033 ripple lengths above the ripple trough.

5.1. *Temporal variations*

Figure 3 shows the variations in concentration with time at increasing elevations above the crest and above the trough, from well within the viscid boundary layer to around half a ripple length above the bed. Concentrations at all locations oscillate at a frequency twice that of the ambient flow and with a magnitude comparable to those of their mean values. Concentrations along the same vertical are roughly in phase, and those above the crest are at a phase shift of a quarter of a wave period from those above the trough. Such temporal variations can be inferred from figure 2 and correspond directly to the locations of the advecting vortices (figure 1).

Other features in figure 3, however, cannot be as easily explained from the vortical flow field. For example, along a vertical through the ripple crest, there is a slight phase lead in local concentration close to the ripple surface. Such a phase lead, however, is not found above the trough. The maxima in concentration have shorter durations

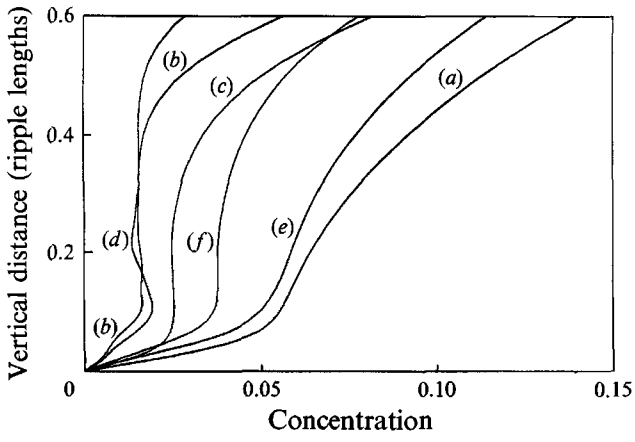

FIGURE 4. Vertical concentration profiles for $s = 0.1$, $R = 1250$, $S = 1$, and $P = 1$. The ordinate is $\tilde{y} - \widetilde{y_r}(\tilde{x})$ (see 2.6). For $P = 1$ ($\nu = \kappa$), the thickness of the Stokes viscid boundary layer and the oscillatory diffusive layer is the same, $O(\delta_s/L) \approx (\nu T)^{1/2}/L = (\kappa T)^{1/2}/L = (\pi/RS)^{1/2} = 0.05$. Profiles (*a*) $t = 122.75$; (*b*) $t = 123$; and (*c*) mean over $122 < t < 123$ are above the crest and profiles (*d*) $t = 122.75$; (*e*) $t = 123$; and (*f*), mean over $122 < t < 123$ are above the trough.

above the crest, and the variation with time is most irregular at about one ripple height above the surface.

5.2. *Vertical profiles*

The time-averaged concentration profiles, both above the crest and above the trough ($122 \leqslant t \leqslant 123$, curves *c* and *f*, figure 4), are typical of the profiles obtained in field measurements (e.g. in Gundersen & Jørgensen 1990). In the layer immediately above the ripple surface, the concentration gradient is nearly linear. Its thickness is of a similar magnitude to that in the diffusive transport over a plane bed under oscillatory flow, $O(\delta_c/L) = 0.05$ (equation (4.3)). The concentration gradients at the crest and the trough are 86% and 35%, respectively, higher than that of the linear profile (3.3).

Above the layer of linear concentration gradient is a region with a concentration that is fairly uniform, and extends to more than two ripple heights above the sediment surface. Apparently this uniform concentration is due to mixing by the vortical flow. Further above where the vortical flow is weak, diffusive transport dominates and the concentration approaches a linear profile. The instantaneous profiles above the crest (curves *a* and *b*, figure 4) and above the trough (curves *d* and *e*), when the ambient velocity is at maximum and at rest, show the large magnitude of temporal variations in local concentration values.†

A linear mean concentration profile in the vertical has often been assumed to be the signature of diffusive-type transport. Figure 1 shows that there is an appreciable vortex-induced normal velocity close to the bottom where the time-averaged concentration gradient is linear (figure 4). Contributions from advective transport can hence be appreciable. Furthermore, there can be net local advective transport in the horizontal over a wave period. I shall quantify this advective transport in §6.3.

† The concentration contours are displaced to the right and to the left over the wave period according to the instantaneous positions of the vortices. The flow cross-section is smallest above the ripple crest and largest above the ripple trough. The vertical concentration gradient is therefore higher above the crest than that above the trough, and the concentration profiles above the crest and above the trough would give the range likely found for profiles in between.

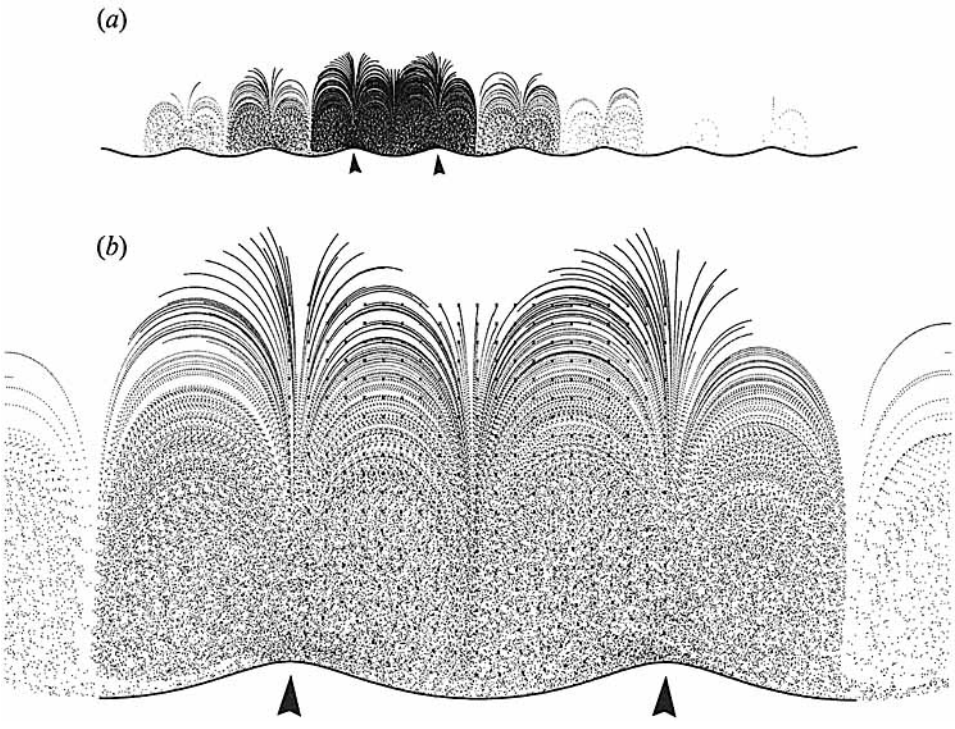

FIGURE 5. Poincaré sections of 420 fluid particles (at $t = 1, 2, 3, ..., 200$) for the time-periodic flow field of $s = 0.1$, $R = 1250$, and $S = 1$. At $t = 0$, the tracer particles are distributed uniformly over a unit square in the mapped plane ($0 \leqslant x \leqslant 1$, $0 < y \leqslant 1$) as marked by the x in (*b*). The ripple length over which the particles are initially placed is between the two arrows below the ripple crests. (*a*) The dispersion of 420 particles in 200 periods; (*b*) an expanded view of the sections over which the ripple length the fluid particles originate.

6. Kinematics of the flow field

Whereas the concentration field presented in §5 reproduces the main features observed in the field measurements of Gundersen & Jørgensen (1990), reliable numerical solutions to the transport equation are feasible only at moderate values of P. To gain further understanding on the characteristics of advective transport in the separated flow above a rippled bed, the kinematic properties of the flow field presented in §4 will be examined. Rom-Kedar, Leonard & Wiggins (1990) analysed quantitatively the mixing properties of a vortex pair in uniform motion in an oscillating strain field, a flow which approaches that of a vortex pair in a wavy-walled channel in the limit when both the separation between the vortices (relative to their distances from the wall) and the amplitude of the wall-waviness are small. Whereas such a flow shares many of the same features as the flow field discussed in §4, it is not obvious how their results can be applied to this more complicated flow. Instead, estimates of mixing efficiency are quantified in §6.3 through an 'equivalent' vertical dispersion coefficient computed from the flow.

6.1. *Poincaré section*

The locations of the same fluid particles at the same phase in succeeding wave periods give a global qualitative description of the nature of mixing by the flow field (Ottino 1989, §§5.5, 7.3.1, 8.2.2). Figure 5 shows the Poincaré section of 420 particles, at

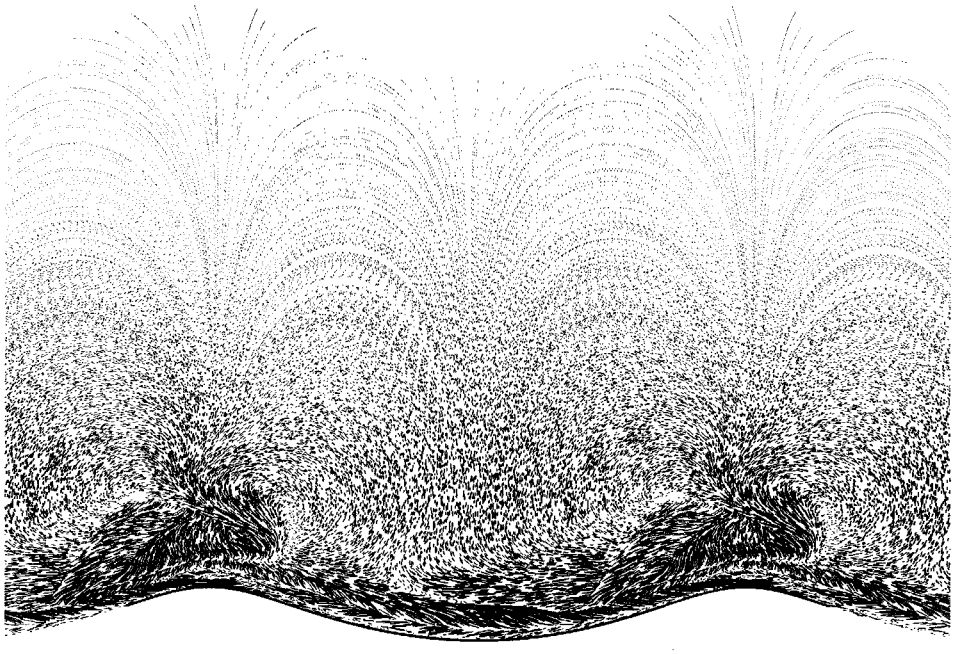

FIGURE 6. Scaled displacements in one wave period of the same 420 particles initially placed as in figure 5 and over half the duration. The displacements are from $t = n$ to $t = n + 1$, $n = 0, 2, 4, ..., 98$. Owing to the large magnitudes of these displacements near the ripple surface, their magnitudes are reduced by a factor of 20. To increase spatial resolution, vectors originating above any ripple length are duplicated above adjacent ripple lengths. Note that the flow field is spatially periodic.

$t = 1, 2, ..., 200$, placed uniformly over one ripple length ($0 \leqslant x \leqslant 1$, $0 < y \leqslant 1$) at $t = 0$. The periodic flow field used is that in the twenty-seventh wave period of computation of (2.1) and (2.2) starting with $\psi = \psi_s$ (3.2) (figure 1).

The fluid particles wander over nine ripple lengths over the duration of simulation and their dispersion is asymmetric on the two sides of the ripple length over which the particles originate. Away from the ripple surface, the net displacements from one period to the next are small. These displacements follow trajectories which are nearly elliptical and reminiscent of the vortical flow shown in figure 1. Immediately above the ripple surface, on the other hand, the section is chaotic. The Poincaré maps at other times, e.g. at $t = n + \frac{1}{4}$, $n = 0, 1, 2, ...$, are qualitatively similar.

Further insights into the mixing characteristics of the flow field can be obtained from a plot of the net displacements of fluid particles in one wave period. The magnitudes and spatial variations of the displacement vectors give a qualitative picture of the local rate of mixing. Figure 6 shows the displacement vectors of the same 420 particles at every other wave period and over half of the duration of figure 5 (i.e. from $t = n$ to $t = n + 1$, $n = 0, 2, 4, ..., 98$). These displacements follow well defined trajectories away from the rippled bed, forming two families of incomplete elliptical trajectories with opposite circulations, each about half a ripple length in width. Close to the ripple surface, however, the displacements are much more complicated. Displacement vectors of large magnitudes extend across the entire ripple length, and vary both vertically and horizontally in their magnitudes and directions. Vortex-like circulations can be identified above the ripple crest.

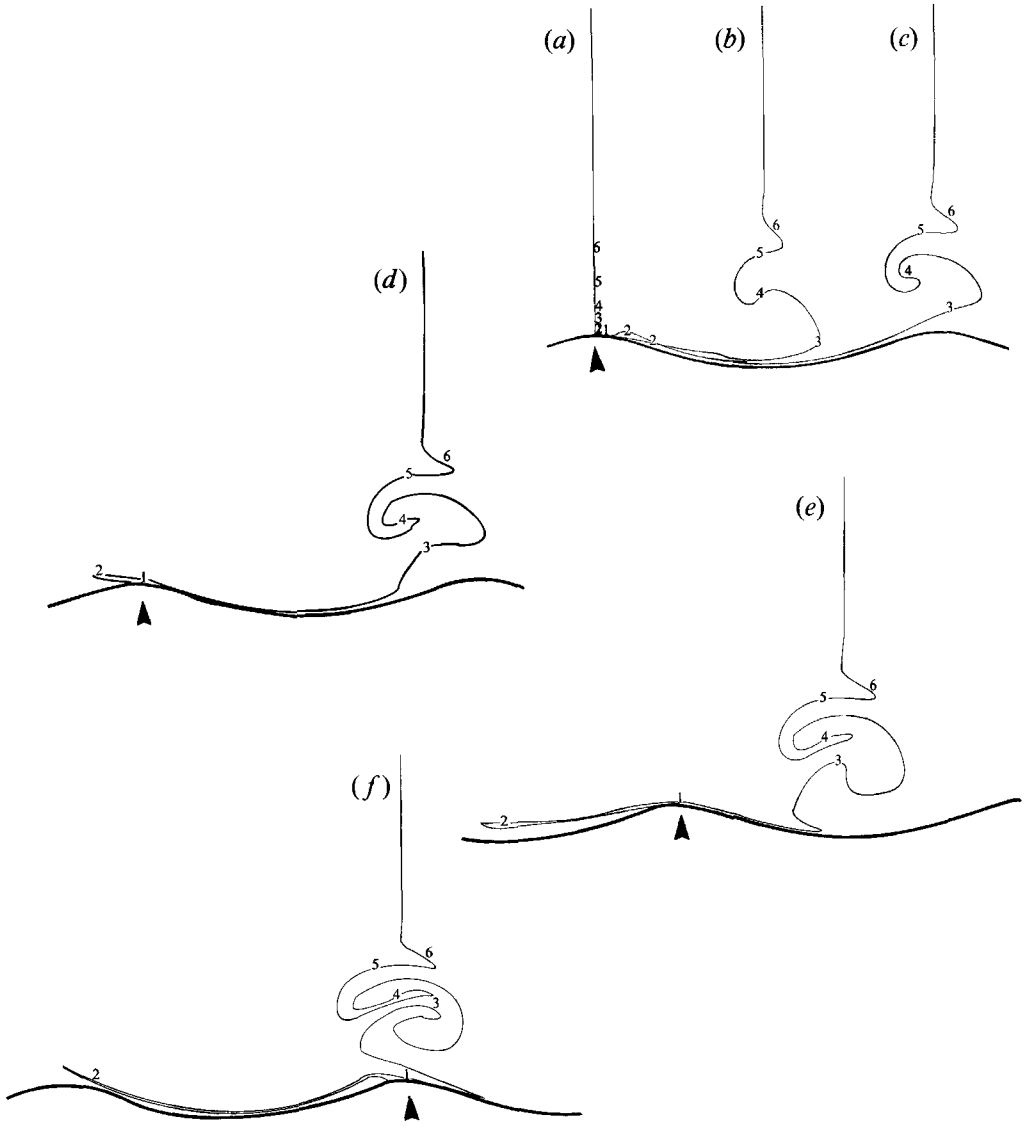

FIGURE 7. Deformation of a vertical line of fluid above a ripple crest over one wave period in the time-periodic flow field of $s = 0.1$, $R = 1250$, and $S = 1$. Markers are placed at distances of 1, 0.0007; 2, 0.0070; 3, 0.0365; 4, 0.0767; 5, 0.1642; and 6, 0.2575 ripple lengths above the crest ($x = 0$, $y = 0.001$, 0.01, 0.05, 0.1, 0.2, and 0.3) at the beginning of the wave period. The arrows mark the ripple crest above which the line of fluid originates. (*a*) $t = 0$, (*b*) $t = 0.25$, (*c*) $t = 0.5$, (*d*) $t = 0.625$, (*e*) $t = 0.75$, (*f*) $t = 1$.

6.2. *Deformation of vertical lines of fluid*

The vortex-like displacements of fluid particles in figure 6 above a ripple crest suggest that the dispersion of fluid particles above ripple crests may be quite different from that above ripple troughs. This can be illustrated by the deformations of vertical line segments of fluid particles above a crest and above a trough.

Two features stand out in the deformation of the vertical line of fluid above a crest in one wave period (figure 7). Close to the ripple surface, the dispersive effects of the coupling of high shear and vortically induced velocity normal to the bed is apparent.

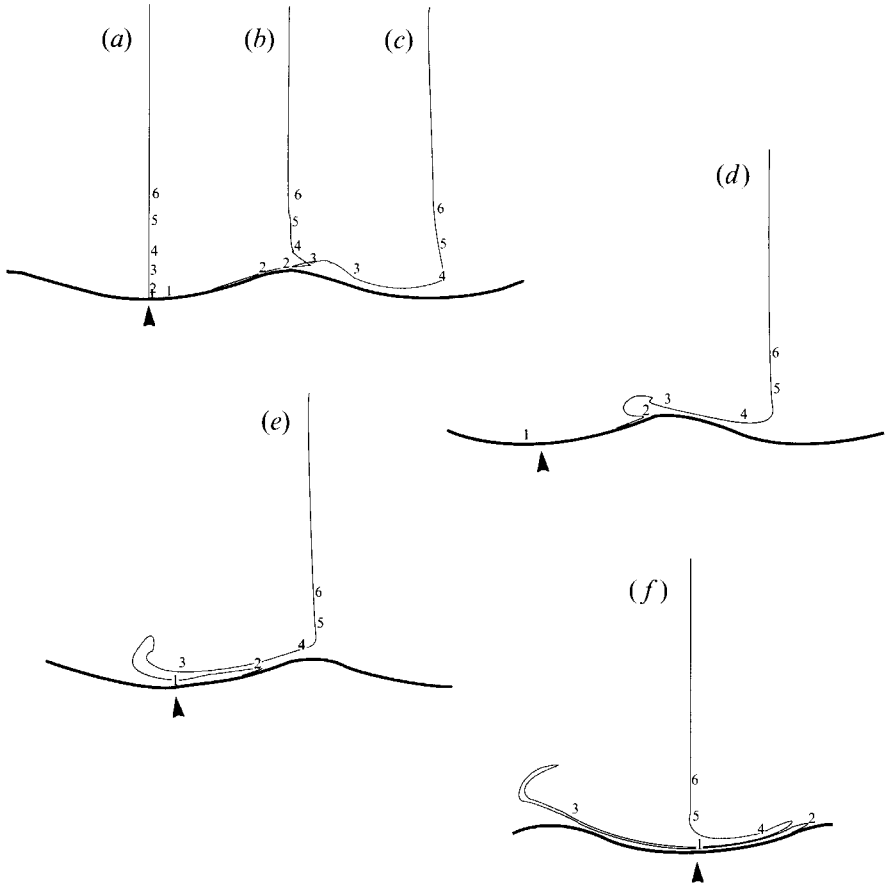

FIGURE 8. Deformation of a vertical line of fluid above a ripple trough over one wave period in the time-periodic flow field of $s = 0.1$, $R = 1250$, and $S = 1$. Markers are placed at distances of 1, 0.0013; 2, 0.0130; 3, 0.0635; 4, 0.1233; 5, 0.2358; and 6, 0.3423 ripple lengths above the trough ($x = 0.5$, $y = 0.001$, 0.01, 0.05, 0.1, 0.2 and 0.3) at the beginning of the wave period. The arrows mark the ripple trough above which the line of fluid originates. (*a*) $t = 0$, (*b*) $t = 0.25$, (*c*) $t = 0.5$, (*d*) $t = 0.625$, (*e*) $t = 0.75$, (*f*) $t = 1$.

The fluid particle labelled 2 is initially at a small distance above the crest, $(x, y) = (0, 0.010)$ or $(\tilde{x}, \tilde{y}) = (0, 0.057)$, and moves very little in the first half-period owing to the small velocity close to the ripple surface. The vortical flow induces a slight upward displacement over this half-period, moving the particle away from the ripple surface where the flow is considerably stronger. Consequently, the particle is convected at close to the velocity of the ambient flow in the second half-period. Fluid particles labelled 1 and 2, originally at a distance of $0.03L$ apart, are now separated by close to a ripple length. The large stretching of the line segment between markers 1, 2, and 3 leads to considerable horizontal mixing immediately above the ripple crest.

Higher up above the bed, vortical motion leads to a roll-up of the line of fluid. The line segments between markers 3 and 5 are stretched and convoluted to a large extent. The resulting lamellar structure entrains neighbouring fluid into a much increased contact area for mixing.

The deformation of a vertical line of fluid above a trough is quite different (figure 8). A point at the same elevation $y = 0.010$ in the mapped plane, or

$(\tilde{x}, \tilde{y}) = (0.500, -0.037)$, is displaced much further in the first half-period than a point at the same elevation above the crest. As opposed to the upward motion induced by the vortices immediately above a crest, the induced movement is downwards. This leads to a smaller horizontal displacement in the second half-period. Higher up, on the other hand, the developing vortex in the second half-period lifts a part of the line segment further away from the bed and leads to a larger displacement in the second half-period. This results in large stretching and the tendril pattern at the end of the wave period. Unlike that above a ripple crest, a vertical line segment of fluid above a trough does not roll up over the course of a wave period.

6.3. *Deformation of horizontal lines of fluid and vertical dispersion*

The question of most interest in this study, from the viewpoint of its application to benthic processes, would be the vertical transport of solutes across the boundary layer. Quantitative estimates of the magnitude of this vertical flux due to advective transport may be obtained from the deformation of horizontal line segments at different elevations from the bottom boundary. The following analysis is performed in coordinates in the mapped plane for expediency. The variation of the 'empirical dispersion coefficients' in the physical plane would be qualitatively similar.

Let $\zeta(x,t)$, $0 \leqslant x \leqslant 1$ and $0 \leqslant t$, be the ordinate of an initially horizontal line in the mapped plane, i.e. $\zeta(x,0) \equiv y_o$. The variance of the vertical displacement of the line segment over a wave period,

$$\kappa_{y_o} = \frac{1}{2} \int_0^1 \mathrm{d}x \, [\zeta(x,1) - y_o]^2, \tag{6.1}$$

gives an 'equivalent diffusion coefficient' due to the vertical dispersion by the flow field (Einstein 1905). In the following numerical computations, the integral in (6.1) is simulated by tracking 30000 points evenly distributed in x between 0 and 1.

The deformation of such a horizontal line of fluid is shown in figure 9 for $y_o = 0.025$. Over one wave period, the line segment stretches and folds at both its ends and also at the centre. The stretching is especially high in the segment between markers 5 and 6 (initially at $x = 0.625$ and 0.75, respectively), as is evidenced from the increase in the lengths of the broken line segments and their separations, both of which have a magnitude of 3.3×10^{-5} initially. Horseshoe patterns are prominent at the end of the wave period.

Deformation of horizontal lines at nearby values of y are qualitatively similar. For horizontal lines of fluids that are initially very close to the bed ($y < 0.01$) or further away from the ripple surface ($y > 0.5$), both the complexities and magnitudes of their deformations in a period are considerably smaller.

Figure 10 is a log-log plot of κ_{y_o} against y_o. Since the mean vertical displacement of the line segment is nonzero, an alternative dispersion coefficient

$$\kappa_{\bar{\zeta}} = \frac{1}{2} \int_0^1 \mathrm{d}x \, [\zeta(x,1) - \bar{\zeta}]^2, \tag{6.2a}$$

where

$$\bar{\zeta} = \int_0^1 \mathrm{d}x \, \zeta(x,1), \tag{6.2b}$$

is also plotted. The variations of κ_{y_o} and $\kappa_{\bar{\zeta}}$ are qualitatively the same, spanning over five orders of magnitude. Both remain fairly constant at their maximum values of $O(10^{-2})$ at $O(y) \approx 10^{-1}$, and decrease monotonically at larger or smaller values of y.

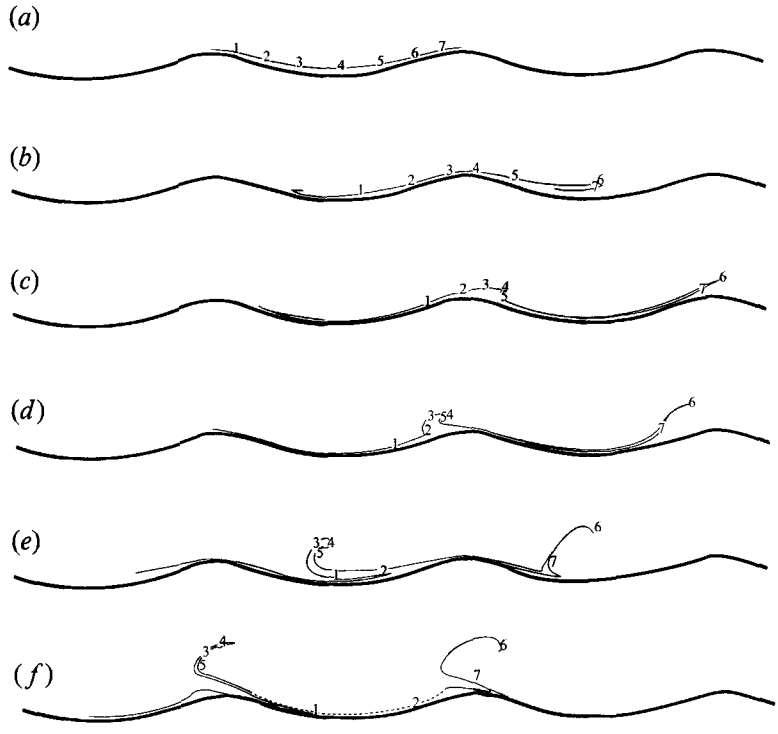

FIGURE 9. Deformation of a horizontal line of fluid particles in the mapped plane over one wave period in the time-periodic flow field of $s = 0.1$, $R = 1250$, and $S = 1$. Markers are distributed evenly over $0 < x < 1$ along the line $y = 0.025$ at the beginning of the wave period, with their coordinates in the physical plane, $(\tilde{x}, \tilde{y})$, at: 1, (0.095,0.055); 2, (0.207,0.025); 3, (0.345,−0.005); 4, (0.500,−0.018); 5, (0.655,−0.005); 6, (0.793,0.025); and 7, (0.905,0.055). (*a*) $t = 0$, (*b*) $t = 0.25$, (*c*) $t = 0.5$, (*d*) $t = 0.625$, (*e*) $t = 0.75$, (*f*) $t = 1$.

As a comparison, the order of magnitude of molecular diffusivity of oxygen, 10^{-9} m^2 s^{-1}, is less than 10^{-7} when nondimensionalized with a ripple length of 0.3 m and a wave period of 6 s. Hence, even in the thin diffusive layer on the ripple profile (with a thickness of $y \approx O(\delta_c/L) \approx 10^{-3}$ for $P = 1000$, equation (4.3)), the vertical dispersion due to a separated flow can be of a magnitude comparable to molecular diffusion.

More importantly, the dispersion coefficients κ_{y_o} and $\kappa_{\bar{\zeta}}$ can be an order of magnitude larger than molecular diffusivity in the region where the time-averaged concentration gradient is linear. For the case of $P = 1$ discussed in §5, the nondimensionalized molecular diffusivity has a value of $\kappa/(L^2/T) \approx 10^{-4}$ for a ripple length of 0.3 m and a wave period of 6 s. Both κ_{y_o} and $\kappa_{\bar{\zeta}}$ exceed 10^{-4} in $0.01 < y < 0.5$, whereas in figure 3, the region of linear concentration extends up to $y \approx 0.05$, at which $O(\kappa_{y_o}, \kappa_{\bar{\zeta}}) \approx 10^{-2}$.

7. Discussion

The role of wave-induced separated flow in the transport of dissolved substances immediately above a rippled bed has been assessed under idealized conditions. The velocity field is time-periodic and composed of two simple flows, one purely oscillatory (ψ_s defined in (3.2)) and one with two persistent vortices above each ripple length.

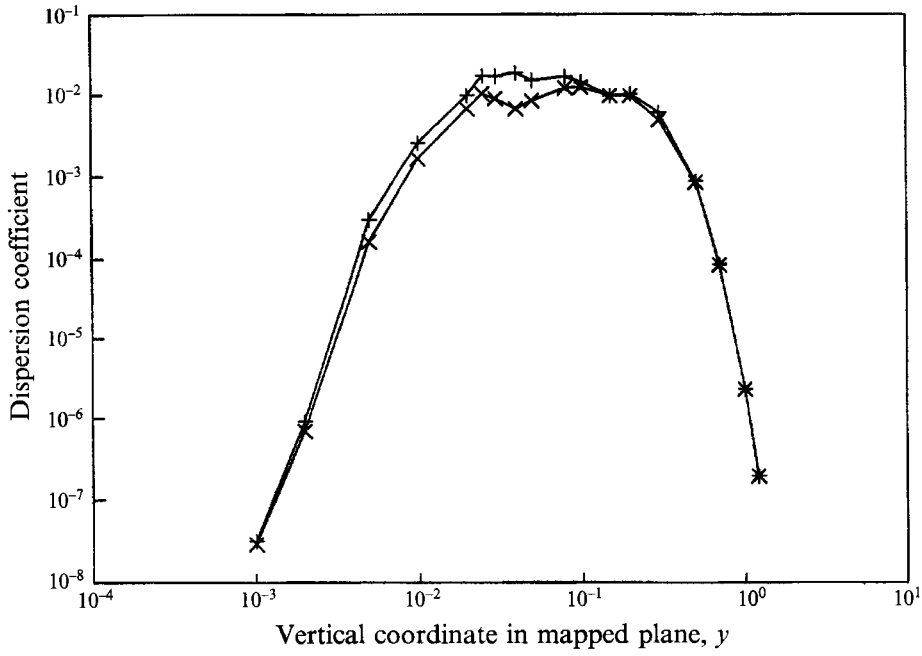

FIGURE 10. Empirical dispersion coefficients as a function of y (ordinate in the mapped plane), estimated from the dispersion of fluid particles over a wave period in the periodic flow field with $s = 0.1$, $R = 1250$, and $S = 1$. The coefficients $\kappa_{y_o}(+)$ and $\kappa_{\bar{\zeta}}(\times)$ are computed from the deformation of an initially horizontal line $y = y_o$ in the mapped plane according to (6.1) and (6.2), respectively. For the nondimensionalization and flow parameters used, the vertical scale of bottom roughness is $y \approx 0.1$, and the thickness of the Stokes viscid boundary layer is $O(\delta_s/L) \approx (\nu T)^{1/2}/L = (\pi/RS)^{1/2} = 0.050$. The thickness of the oscillatory diffusive layer is, for $P = 1$ or $\kappa_1 = \nu = 10^{-6}$ m^{2}s^{-1}, $O(\delta_c/L) \approx (\kappa_1 T)^{1/2}/L = (\pi/PRS)^{1/2} = 0.05$, and for $P = 10^3$ or $\kappa_2 = 10^{-9}$ m^{2}s^{-1}, $O(\delta_c/L) \approx 0.0016$. Nondimensionalized molecular diffusivity of oxygen is $\kappa_1/(L^2/T) \approx 10^{-4}$ for $P = 1$ and $\kappa_2/(L^2/T) \approx 10^{-7}$ for $P = 10^3$ for a ripple length of 0.3 m and a wave period of 6 s.

During each half-period, the vortex generated at the lee of a ripple crest merges with one of the two existing vortices advecting with the oscillatory flow.

Material lines of fluid deform in complicated patterns which vary considerably both along the ripple length and with increasing distance from the bed. The boundary-generated vortical flow induces an advective transport normal to the bed. Close to the sediment surface, this normal velocity couples with the high shear and results in large net displacements of fluid particles in one wave period. Such fluid motions lead to an efficient mixing mechanism.

The magnitude of advective transport can be significantly higher than molecular diffusion in the region from within the 'diffusive boundary layer' to a height of a ripple length from the bed. A diffusive boundary layer (DBL) is commonly assumed to be the layer immediately above a sediment bed where the time-averaged concentration gradient in the vertical is linear, and solute transport within the DBL has often been estimated using a diffusion-type model in field and laboratory studies in geochemistry. Results in §§5 and 6 show that, owing to advective transport and the two-dimensional nature of the physical system, a linear mean concentration gradient does not warrant a one-dimensional diffusion-type transport model.

Advective transport can also lead to significant dispersion in the horizontal. Fluid

particles originating from above one single ripple length can be found above nine adjacent ripple lengths over the course of the subsequent 200 wave periods (figure 5). Line segments of fluid that are initially vertical are also deformed considerably at the end of a wave period (figures 7 and 8). An 'equivalent diffusion coefficient' in the horizontal would be orders of magnitude higher than that of molecular diffusivity (but its value would vary with the vertical extent of the fluid element used in computing such an estimate).

Limitations on available computation resources have restricted the present study to flows considerably weaker than those commonly found in the field.† For example, the dimensionless parameters give $RS = \pi L^2/(\nu T) \approx 47000$ for $L = 0.3$ m, $T = 6$ s, and $s = 0.1$. If R is to be kept sufficiently low to achieve numerical accuracy, S would have to be so high that the resulting vortical flow would be insignificant. The parameters in this study, $R = 1250$, $S = 1$ and $s = 0.1$, give $U^2T = 125\pi\nu/s \approx 4 \times 10^{-3}$. For a ripple height of even as low as 1 cm, this would require $U < 1.3$ cm s^{-1} and $T > 25$ s. Nevertheless, this weak but separated flow reveals many characteristics of chaotic mixing such as tendrils, whorls, and Smale horseshoe structures, and is relatively simple to study owing to its temporal and spatial periodicities. I believe that the same qualitative features of solute transport found in the present study would also be present at higher values of the dimensionless parameters.

Local concentration values oscillate at twice the wave frequency (figure 3) whereas those measured in coastal water by Gundersen & Jørgensen (1990) oscillate at the wave frequency. This difference may be due to an irregular topography at the site the measurements were made, for example if vortices were shedded from one side of the probe only. The results of §5 show that the concentration field is sensitive to the positions of the vortices, and both Blondeaux & Vittori (1991*a*) and Shum (1988) found that the trajectories of the boundary-generated vortices vary considerably with flow conditions (the Reynolds number and the Strouhal number). Given the limited range of flow parameters these numerical solutions can resolve at present, laboratory experiments appear to be a more promising approach to resolve the discrepancy.

As this study is focused on the vortical flow generated at the bottom boundary, contributions to solute transport due to ambient turbulence have not been modelled. In the present model, the downward flux of solutes near the upper boundary of the computational domain is due to diffusion. In the field, ambient turbulence dominates vertical solute transport away from the bed and a more uniform solute concentration can be expected.

The sediment surface has been assumed to be impermeable and at a constant solute concentration for expediency. Shum (1992) showed that the wave-induced pore water flow can lead to a percolation pattern that varies appreciably both within the wave period and along the ripple length. Hence, the deformation of fluid elements presented in §6 may be different when percolation effects are important. To properly account for the effects of percolation would require orders of magnitude increase in computational efforts, however. The pore water flow field depends on a number of factors, among them the ratio of gravity wavelength to the thickness of the permeable sediment layer. Straightforward coupling of (2.1) and (2.2) to the pore water flow below the rippled bed would therefore require a computational domain with a horizontal extent that of the gravity wavelength.

The boundary solute concentration may also vary along the ripple surface. For

† See for example Dingler & Inman (1976) for typical ripple dimensions as a function of ambient flow conditions.

the case of a solute being consumed inside the sediment according to first-order reaction kinetics, Shum (1993) showed that the wave-induced pore water flow may lead to a much lower solute concentration immediately below a ripple crest than that immediately below a trough. The variation in boundary concentration increases with the magnitude of pore water flow and would alter the concentration field discussed in §5. The modifications needed in the numerical model to account for a variable bottom boundary concentration, however, is straightforward.

Advective transport is shown to dominate even in the so-called 'diffusive boundary layer' in a separated oscillatory boundary layer. Further numerical and experimental studies are needed to explore how variations in turbulence level would influence this transport characteristic. Aside from applications to benthic processes in geochemistry, these results may also help in furthering our understanding in other fields such as marine biology (e.g. boundary layers around organisms, Lazier & Mann 1989) and heat transport (e.g. cooling over ribbed surfaces).

Another related problem of interest is the mixing due to eddies generated around headlands or other coastline features. Results in §6 show that the dispersion due to boundary-generated vortices can be highly variable in space, and this dispersion is likely to be quite sensitive to the flow parameters. In numerical ocean circulation models, a diffusion-type model may therefore not be sufficient to describe the dispersion near land boundaries when coastal features with a length scale of or smaller than the grid size are present.

Appendix. The equivalence of (2.10) to an imposed oscillatory pressure gradient

The flow field examined in this study is driven by an oscillatory ambient pressure gradient. In the streamfunction/vorticity formulation, this boundary pressure is not imposed explicitly. As no boundary conditions are needed for the vorticity, no further conditions on the far-field velocity (e.g. $\omega = 0$) could have been imposed to dictate an oscillatory ambient flow (as opposed to an oscillating upper boundary). Nevertheless, the boundary conditions (2.10) at $y = y_{max}$ impose an oscillatory pressure gradient in the far field, which can be seen as follows.

Consider Navier–Stokes equations in the horizontal direction, nondimensionalized as in §2 and pressure scaled with ρU^2,

$$\frac{\partial \tilde{u}}{\partial t} + \frac{\pi}{S}\left(\tilde{u}\frac{\partial \tilde{u}}{\partial \tilde{x}} + \tilde{v}\frac{\partial \tilde{u}}{\partial \tilde{y}}\right) = -\frac{\pi}{S}\frac{\partial p}{\partial \tilde{x}} + \frac{\pi}{RS}\left(\frac{\partial^2 \tilde{u}}{\partial \tilde{x}^2} + \frac{\partial^2 \tilde{u}}{\partial \tilde{y}^2}\right). \tag{A 1}$$

Recall that variables with tildas are those in the physical plane. High above the rippled bed,

$$\tilde{u} = \frac{\partial \psi}{\partial \tilde{y}} \approx \frac{\partial \psi}{\partial y}, \quad \tilde{v} = -\frac{\partial \psi}{\partial \tilde{x}} \approx -\frac{\partial \psi}{\partial x} \tag{A 2a,b}$$

where unscripted variables (x, y) are those in the mapped plane. The approximations hold for $y = O(1)$ and follow from the conformal mapping (2.7) and (2.8) and the identities

$$\frac{\partial \psi}{\partial \tilde{x}} = \frac{1}{J}\left(\frac{\partial \tilde{x}}{\partial x}\frac{\partial \psi}{\partial x} - \frac{\partial \tilde{y}}{\partial x}\frac{\partial \psi}{\partial y}\right) \tag{A 3a}$$

and

$$\frac{\partial \psi}{\partial \tilde{y}} = \frac{1}{J}\left(\frac{\partial \tilde{x}}{\partial x}\frac{\partial \psi}{\partial y} + \frac{\partial \tilde{y}}{\partial x}\frac{\partial \psi}{\partial x}\right). \tag{A 3b}$$

Substitution of (A 2) into (A 1) and evaluation at $y = y_{max}$ with boundary conditions (2.10) gives

$$\frac{\partial p}{\partial \tilde{x}} = -\frac{S}{\pi}\frac{\mathrm{d}}{\mathrm{d}t}U_\infty(t) + \frac{1}{R}\frac{\partial^3 \psi}{\partial y^3}. \tag{A 4}$$

The second term on the right-hand side of (A 4) is orders of magnitude smaller than the first term since $1/R < 10^{-3}$ in this study, and $\partial^3\psi/\partial y^3 \approx -\partial\omega/\partial y$ at $y = y_{max}$ is $O(\delta^2)$ as computed by the finite-differencing scheme with vertical spacing δ.

Therefore, to a good approximation, (A 4) reads

$$\frac{\partial p}{\partial \tilde{x}} = -\frac{S}{\pi}\frac{\mathrm{d}}{\mathrm{d}t}U_\infty(t). \tag{A 5}$$

That is, the pressure gradient $\partial p/\partial x$ is that due to an oscillatory far-field velocity $U_\infty(t)$.

REFERENCES

ANDERSON, D. A., TANNEHILL, J. C. & PLETCHER, R. H. 1984 *Computational Fluid Mechanics and Heat Transfer*. Hemisphere.

BENJAMIN, T. B. 1959 Shearing flow over a wavy boundary. *J. Fluid Mech.* **6**, 161–205.

BLONDEAUX, P. & VITTORI, G. 1991*a* Vorticity dynamics in an oscillatory flow over a rippled bed. *J. Fluid Mech.* **226**, 257–289.

BLONDEAUX, P. & VITTORI, G. 1991*b* A route to chaos in an oscillatory flow: Feigenbaum scenario. *Phys. Fluids* A 3, 2492–2495.

CARSLAW, H. S. & JAEGER, J. C. 1963 *Operational Methods in Applied Mathematics*. Dover.

DINGLER, J. R. & INMAN, D. L. 1976 Wave-formed ripples in nearshore sands. In *Proc. 14th ASCE Coastal Engineering Conference*, pp. 2109–2126.

DU TOIT, C. G. & SLEATH, J. F. A. 1981 Velocity measurements close to rippled beds in oscillatory flows. *J. Fluid Mech.* **112**, 71–96.

EINSTEIN, A. 1905 Über die von der molekularkinetischen Theorie der Wärme geforderte Bewegung von in ruhenden Flüssigkeiten suspendierten Teilchen. *Annln Phys.* 17, (47), 549–560. (In German)

GHADDAR, N. K., MAGEN, M., MIKIC, B. B. & PATERA, A. T. 1986 Numerical investigation of incompressible flow in grooved channels. Part 2. Resonance and oscillatory heat-transfer enhancement. *J. Fluid Mech.* **168**, 541–567.

GUNDERSEN, J. K. & JØRGENSEN, B. B. 1990 Microstructure of diffusive boundary layers and the oxygen uptake of the sea floor. *Nature* **345**, 604–607.

HARA, T. & MEI, C. C. 1992 Oscillating flows over periodic ripples of finite slope. *Phys. Fluids* A **4**, 1373–1384.

LAZIER, J. R. N. & MANN, K. H. 1989 Turbulence and the diffusive layers around small organisms. *Deep-Sea Res.* **36**, 1721–1733.

MEI, C. C. & LIU, P. L.-F. 1993 Surface waves and coastal dynamics. *Ann. Rev. Fluid Mech.* **25**, 215–240.

OTTINO, J. M. 1989 *The Kinematics of Mixing: Stretching, Chaos, and Transport*. Cambridge University Press.

ROM-KEDAR, V., LEONARD, A. & WIGGINS, S. 1990 An analytical study of transport, mixing and chaos in an unsteady vortical flow. *J. Fluid Mech.* **214**, 347–394.

SCHLICHTING, H. 1968 *Boundary Layer Theory*. McGraw Hill.

SHUM, K. T. 1988 A numerical study of vortex dynamics over rigid ripples. Doctoral thesis, MIT.

SHUM, K. T. 1992 Wave-induced advective transport below a rippled water-sediment interface. *J. Geophys. Res.* **97**, 789–808; and Corrections, **97**, 14475–14477.

SHUM, K. T. 1993 The effects of wave-induced pore water circulation on the transport of reactive solutes below a rippled sediment bed. *J. Geophys. Res.* **98**, 10289–10301.

SOBEY, I. J. 1985 Dispersion caused by separation during oscillatory flow through a furrowed channel. *Chem. Engng Sci.* **40**, 2129–2134.

TA PHUOC LOC 1980 Numerical analysis of unsteady secondary vortices generated by an impulsively started circular cylinder. *J. Fluid Mech.* **160**, 93–117.

THORSNESS, C. B. & HANRATTY, T. J. 1979 Mass transfer between a flowing fluid and a solid wavy surface. *Am. Inst. Chem. Engng J.* **25**, 686–697.

VITTORI, G. & TANDA, G. 1991 Study of separated flow and heat transfer in two-dimensional channels with wavy walls. In *Proc. 24th Congress of Intl Assoc of Hydraulic Res. Madrid, Spain*, pp. C203–C210.